Mechanisms of the Overturning Circulation in the Northern Red Sea, more than Convective Mixing

Lina Eyouni[1,2], Zoi Kokkini [1,3], Nikolaos D. Zarokanellos [1,4], Burton H. Jones [1]

[1] King Abdullah University of Science and Technology (KAUST), Biological and Environmental Sciences and Engineering (BESE), Red Sea Research Center (RSRC), Thuwal, Saudi Arabia.
[2] Red Sea Global (RSG), Riyadh, Saudi Arabia.
[3] Consiglio Nazionale Delle Ricerche (CNR), Istituto di Scienze Marine (ISMAR), Lerici, Italy
[4] Balearic Islands Coastal Observing and Forecasting System (SOCIB), Palma de Mallorca, Spain

Correspondence to: Zoi Kokkini (zoi.kokkini@sp.ismar.cnr.it)

Abstract. The northern Red Sea (NRS) is where Red Sea Outflow Water and, occasionally, Red Sea Deep Water, are formed. Glider observations are used to describe the formation mechanisms and pathways of the intermediate waters in the NRS in late winter from 31 January to 18 April 2019. Utilizing glider observations, atmospheric reanalysis products, and satellite datasets, we evaluated the mesoscale activity and the atmospheric conditions that contribute to outflow water formation. The cyclonic circulation in the region surfaces dense water, which exposes it to the atmosphere, ventilating the water column and contributing to phytoplankton growth (enhancement of chlorophyll concentration) due to the nutrients upwelled into the euphotic zone. Subduction of this water in the 3-dimensional cyclonic circulation transported oxygenated, elevated chlorophyll water to depths between 150 m and 250 m along the 28.2 kg/m3 isopycnal. Unlike previous observations, in late February, a strong anticyclonic circulation blocked the inflow of warmer, fresher water into the region. It was accompanied by a negative heat flux and an uplifting of dense water to the surface. Net cooling through mid-March cooled the incoming surface waters from the south. At the end of the observational period, the intrusion of warmer, fresher waters from the south coincided with the re-establishment of cyclonic circulation and capped the dense surface water that had formed during March. These observations demonstrate that multiple processes contribute to Red Sea Outflow Water formation - convective mixing, cyclonic uplifting of dense water, subduction, and meso(submeso-)scale processes.

1 Introduction

The Red Sea (RS) is a narrow, elongated, meridionally oriented basin lying between the Asian and African continents. Its subtropical location results in significant buoyancy losses due to high evaporation (nearly 2 m/yr), negligible precipitation, and effectively no riverine inputs, resulting in it being one of the world's saltiest and warmest seas (Edwards and Head, 1987;

Smeed, 1997; 2004; Sofianos et al., 2002). The RS experiences seasonally reversing winds over the southern region, coupled with the Arabian Sea's monsoonal forcing. The reversing winds control the circulation and water mass exchange through the Strait of Bab al Mandab (Abualnaja et al., 2015; Patzert, 1974). These processes, along with the buoyancy forcing, drive the large-scale circulation (Bower and Farrar, 2015; Murray and Johns, 1997; Patzert, 1974; Sofianos and Johns, 2007). The inflow of water from the Gulf of Aden compensates for the evaporative water loss in the RS. The advected northward waters contribute to the overall latitudinal gradient in salinity and temperature from the south to the north. The northward advection of comparatively fresh and warm water from the south has an important role in the stratification (Asfahani et al., 2020; Churchill et al., 2014; Sofianos and Johns, 2007; Zarokanellos et al., 2017b), with the annual flux into the Red Sea reaching up to 0.22 Sv (Sofianos and Johns, 2002). This water has been traced to the NRS at 28˚N (Zarokanellos et al., 2017a). It is modified through heating, evaporation, and mixing as it progresses northward (Cember, 1988; Sofianos and Johns, 2003; Sofianos and Johns, 2007).

Significant mesoscale activity is found along the RS's main axis (Morcos, 1970; Morcos and Soliman, 1972; Quadfasel and Baudner, 1993; Sofianos and Johns, 2007; Zhan et al., 2014) that results from baroclinic instabilities (Zhan et al., 2014) and the presence of the Eastern Boundary Current (EBC; Zarokanellos et al., 2017a, 2017b; Biton et al., 2010; Biton et al., 2008; Bower and Farrar, 2015; Eshel et al., 1994; Eshel and Naik, 1997; Sofianos and Johns, 2007). Some of these mesoscale eddies are thought to be quasi-permanent features, in particular the cyclonic eddy (CE) in the NRS and the anticyclonic (AE) in the Central Red Sea (CRS) (Chen et al., 2014; Yao et al., 2014b). The CE in the NRS plays a crucial role in forming the RSOW (Asfahani et al., 2020; Sofianos and Johns, 2007). Zarokanellos et al. (2017a) have shown that an AE in the CRS can redirect or deflect the advected northward flow of Gulf of Aden water. These mesoscale eddies substantially affect heat and salt advection and distribution of biogeochemical properties (Chen et al., 2014; Raitsos et al., 2013; Triantafyllou et al., 2014), which are often useful tracers of physical processes. Eddies also transfer energy and momentum to the mean flow, driving the circulation (Lozier, 1997).

Water mass transformation typically occurs in the surface ocean in specific regions where air-sea interaction acts powerfully on the upper layer (Emery, 2001; Iselin, 1939). Significant surface cooling results in buoyancy loss that can contribute to deep mixing and convection. The NRS has been considered the main area of RSOW formation and, occasionally, Red Sea deep water (RSDW) formation (Papadopoulos et al., 2015; Sofianos and Johns, 2003; Sofianos and Johns, 2007; Yao et al., 2014 b), due to the high evaporation rates and significant surface water cooling that occur during winter (Papadopoulos et al., 2013). These preconditions, in addition to the presence of the CE, where shallowing of the isopycnals occurs at the eddy center, contribute to the formation of the aforementioned RSOW and RSDW (Abualnaja et al., 2015; Asfahani et al., 2020; Sofianos and Johns, 2003; Yao et al., 2014 b; Zhai et al., 2015). The newly formed RSOW gradually sinks until it reaches an equilibrium density of near 27.5 to 27.7 kg/m^3 throughout the basin (Zhai et al., 2015) and flows southward, where it exits the Red Sea through the strait of Bab-El-Mandeb (Cember, 1988; Sofianos and Johns, 2003; Yao et al., 2014 b). Once it enters the Gulf of Aden, it is mixed due to the intense mesoscale eddy activity at depths between 400 and 1000 m (Bower and Furey, 2010). Despite significant dilution of the thermohaline properties, RSOW has been observed as far southward as the Agulhas Current

65   below 32˚S (Beal et al., 2000) and as far east as the Bay of Bengal (Jain et al., 2017). Numerical simulations and a few in-situ observations suggest three potential mechanisms for RSOW formation. The first mechanism, open-ocean convection, is associated with the presence of a cyclonic gyre in the NRS (Sofianos and Johns, 2007; Papadopoulos et al., 2015). Strong atmospheric forcing in the region and the presence of the cyclonic gyre creates favorable conditions for convection events. The second mechanism is mixed layer deepening during winter, resulting from a large negative heat flux (Zhai et al., 2015).

70   The third mechanism is the combined effect of the cyclonic gyre and the weakening of the stratification that results from strong atmospheric forcing (Chen et al., 2014; Clifford et al., 1997; Manasrah et al., 2004; Morcos and Soliman, 1972; Yao et al., 2014 b). Concurrent with the formation of the RSOW, the RSDW forms in the NRS when strong cooling and evaporation occur in the gulfs of Suez and Aqaba (Cember, 1988; Papadopoulos et al., 2015; Sofianos and Johns, 2003; Yao et al., 2014 b). The RSDW is evident below 300 m, while the RSOW is typically found between 200 m and 300 m and can be identified

75   by the relatively high oxygen concentration, which can be distinguished from the RSDW. The regionally formed RSOW has a significant role in the overturning circulation, as indicated by in-situ observations and numerical simulations (Papadopoulos et al., 2015; Sofianos and Johns, 2003; Zhai et al., 2015). In addition, RSOW contributes to the ventilation of the Red Sea (Papadopoulos et al., 2015; Sofianos and Johns, 2007; Woelk and Quadfasel, 1996; Yao et al., 2014 b; Zhai et al., 2015) and the salt budget of the Indian Ocean due to the high salinity concentrations present in intermediate depths (Beal et al., 2000).

80   The primary objective of this study is to understand the mechanisms that contribute to the mass formation of RSOW in the NRS and the biogeochemical responses associated with these physical processes. The second objective is to evaluate how atmospheric forcing affects mesoscale dynamics in the study area. This paper is organized as follows: In Section 2, the in-situ, reanalysis, and remote sensing observations are presented. Section 3 describes the coupling of the atmospheric forcing and the in-situ observations. A comprehensive description of the flow variability and the mechanism of RSOW formation is described,

85   including the coupling between physical and biogeochemical processes in the study areas. Lastly, discussion and conclusions are presented in Section 4.

2 Data and methods

2.1 Glider observations

A sustained glider line that was traversed in a 3-4 day period in the NRS was used to capture the wintertime evolution of

90   physical and biogeochemical characteristics in the northern Red Sea (Eyouni et al., 2024). The Seagliders (hereinafter "gliders") were equipped with a CTD, a dissolved oxygen sensor, and a triplet fluorometer (Table 1). The glider was deployed along a transect oriented approximately perpendicular to the coastline offshore from Duba, referred to as the "Duba line" (Fig. 1a). The line extended from approximately 5 km off the coast to nearly 75 km offshore. The glider completed each transect in about 3.5 days and was programmed to dive from the surface to ~750 m. The average horizontal speed was ~25 cm/s, and each

95   dive cycle took ~3 hours to complete, depending on the target depth, topography, and sea conditions. The deployment spanned the period from 31 January to 21 April, 2019 (Table 1, Fig. 1b).

Deployment Location	Observation Period	Duration (days)	Sensors	Parameter
NRS	30.01.2019/22.04.2019	83	Seabird, unpumped CT	CTD (Conductivity, Temperature, Pressure)
			Seabird EcoPuck Fluorometer (FL3)	Chlorophyll Fluorescence (CHL) Colored Dissolved Organic Matter (CDOM) Phycocyanin
			Aanderaa Optode (4330)	Dissolved Oxygen (DO)

Table 1: Summary of the measured variables and their corresponding sensors deployed on the glider.

100
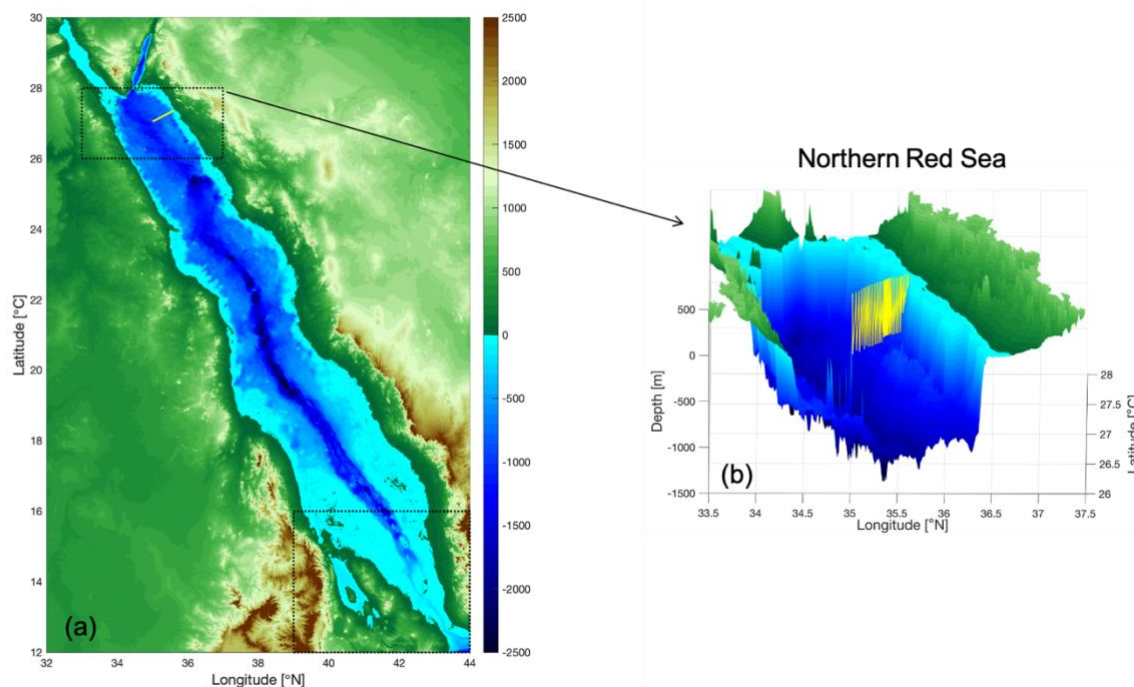
Figure 1: Topographic map of the Red Sea. The two black dash boxes in the northern and southern Red Sea show the study area in the north and the region in the south where exchange with the Gulf of Aden occurs. The yellow line inside the northern box indicates the glider line location, and b) the yellow sawtooth line represents the undulating trajectory of the glider superimposed on the
105 **bathymetry, which has been reproduced from the GEBCO_2021 Grid, GEBCO Compilation Group (2021; https://doi.org/10.5285/c6612cbe-50b3-0cff-e053-6c86abc09f8f).**

Each vertical profile has been examined for spikes and outliers before further analysis. No evidence of thermal lag has been observed in the CT observations. The Seabird EcoPuck Triplet Fluorometer (FL3) sensor was factory calibrated, and dark
110 counts were measured prior to deployment to account for any drift. The pre-deployment dark counts were consistent with factory dark counts. Roesler et al. (2017) performed a global comparison of fluorometer and extracted CHL measurements and recommended that factory-calibrated CHL be divided by 2 to correspond to in situ CHL concentrations. The oxygen measurements were adjusted by a correction factor based on the median oxygen saturation in the upper 10 m. The correction factor was the ratio of the median oxygen saturation concentration for the upper 10 m to the median measured concentration
115 within the upper 10 m of the water column. The entire water column data was then corrected by multiplying the reported oxygen concentrations by the correction factor. The correction provided consistency between the current glider data set and the vertical distribution for this region in the World Ocean Atlas (Zarokanellos and Jones, 2021; Garcia et al., 2019). To

facilitate data processing, plotting, and analysis, the corrected data were projected onto a grid with a vertical resolution of 2 m
and a horizontal resolution of 2.5 km, the nominal distance between glider surfacings during the mission. This study focuses

120   on the upper 500 m of the water column. Mixed Layer Depth (MLD) was calculated for each vertical profile based on a density
difference of ≤ 0.03 kg/m^3 relative to the density at 10 m depth (de Boyer Montégut et al., 2004). The Brunt-Vaisala frequency
(BVF) was computed to measure stratification. Geostrophic velocity and potential density were also calculated using the
TEOS-10 toolbox (TEOS, SCOR, and IAPSO, 2010). The level of no motion in the geostrophic velocity has been examined,
and no significant motion below 500m has been observed.

125

2.2 Remotely sensed data

2.2.1 Sea Level Anomaly (SLA)

Previous satellite observations and numerical simulation studies suggest a cyclonic gyre located in the NRS concurrent with
convective mixing where the RSOW water mass is formed (Sofianos and Johns, 2002; Zhai et al., 2015). Therefore, in this

130   study, SLA data were used to characterize the spatial and temporal evolution of the large-scale circulation patterns of sea level
and geostrophic velocity during the wintertime. The SLA data is based on the multi-mission altimeter Archiving Validation
and Interpretation of Satellite Oceanographic Data (AVISO) provided by the Copernicus Marine Environment Monitoring
Service (CMEMS). The data has been gridded at a regular $0.258° \times 0.258°$. The obtained daily measured data were taken
within the domain from 20° to 28° N and 32° to 42° E, inclusive of the glider deployments. Within the NRS subdomain (26

135   - 28°N, 33 - 37°E) the data were temporally averaged to fit approximate the periods of the glider transects. Previous work has
validated the use of the AVISO product from comparisons with both in situ and numerical model results (Hernandez and
Schaeffer, 2001; Zhan et al., 2014; Zarokanellos et al., 2017).

2.2.2 Sea Surface Temperature (SST)

Sea surface temperature (SST) data were obtained from the Moderate Resolution Imaging Spectroradiometer (MODIS)

140   imagery that provides a daily image with a spatial resolution of 4 km. The data were obtained within the domain from 24° to
28° N to identify and determine the spatial and temporal evolution of the large-scale patterns of the SST (Werdell et al., 2013).

2.3 Atmospheric reanalysis products

The Modern-Era Retrospective Analysis for Research and Applications Version 2 (MERRA-2) was used to provide daily mean

145   values of the atmospheric parameters with a spatial resolution $0.5° \times 0.652°$ grid and a temporal resolution of one hour
(Rienecker et al., 2011; Gelaro et al., 2017). The data were extracted within a spatially averaged box over the NRS (26 - 28
°N, 33 - 37 °E; Fig. 1a), excluding land coverage. Daily means were calculated from the hourly data for the selected parameters

of wind speed and direction, surface net heat flux (Q_{net}), and evaporative heat flux, which is considered to be the primary driver of heat loss in the Red Sea (Sofianos ad Johns, 2003).

150 The Q_{net}, produced using the Coupled Ocean-Atmosphere Response Experiment (COARE 3.0) formulation (Fairall et al., 1996), consists of the sum of shortwave (Q$_{sw}$, absorbed), longwave (Q$_{lw}$, emitted), latent (Q$_L$, evaporative), and sensible (Q$_s$, conductive) heat fluxes, as all terms are positive when they are heating the water column. The quantity Q_{net} is calculated using the following formula:

155 $$Q_{net} = Q_{sw} + Q_{lw} + Q_S + Q_L \tag{1}$$

2.4 Empirical Orthogonal Function (EOF) analysis

To compare the SLA from 2019 with observations from the preceding years, EOF analysis is carried out on SLA data to evaluate the spatial and temporal patterns of the variability of the SLA data in the winter-spring period. Each eigenvector

160 describes the spatial pattern (modes) of that variability for five months of January to May for the years 2016, 2017, 2018, and 2019. Only the first mode of the EOF is used to compare the seasonal evolution of the spatial pattern each year. In addition, the explained variance with the eigenvalue provides the relative contribution that a specific mode contributes to the variability (Zhang and Moore, 2015).

165 ## 2.5 One-dimensional mixed layer model

Price-Weller-Pinkel (PWP) mixed layer model (Price et al., 1986) has been applied to evaluate the local atmospheric effects on the ocean mixed layer. The. The model input includes the following terms: radiative heat flux (shortwave, longwave), latent and sensible heat, freshwater flux (evaporation [E] and precipitation [P]; [$E - P$]), and wind stress components [τ_x and τ_y]). As the Red Sea is sandwiched between two extreme desert regions, precipitation is considered to be negligible (P=0). The 1-

170 D PWP has been applied to estimate the local, atmospherically-driven evolution of the mixed layer depth during the observation period. The model was executed for three sequential subsets delineated from the glider observations: the cooling phase, the cool, salty, dense phase, and the warming-freshening phase. The model was initialized with the average temperature and salinity profile for one complete glider transect at the beginning of each simulation period (30 days) and then stepped forward in 24-hour (1-day) increments subject to the heat, freshwater, and momentum fluxes. The daily time step was selected as

175 insignificant diurnal variability was observed in mixed layer temperature and salinity from the glider.

The PWP model produces a mixed layer through a vertical exchange process between the air and sea interaction, and vertical mixing. It assimilates time series of surface heat flux, wind, and precipitation, and applies these forcing parameters to the initial vertical profile of temperature and salinity. The model interpolates the momentum components driven by winds, cooling, and

evaporation to induce convective instability, entrainment from the pycnocline, and a mixing term generated from vertical current shear. In our case, since P=0, only surface heating affects re-stratification.

The convective adjustment in the PWP model starts with grid cells with unstable stratification being homogeneously blended with neighboring cells. The convective correction follows the bulk mixed layer parameterization, where the mixed layer deepens when the bulk Richardson number, R_{ib}, falls below a threshold value of 0.65 (Price et al., 1986). The bulk Richardson number is expressed as: $R_{ib} = \frac{\Delta \rho g}{\rho_0 (\Delta U)^2}$ (2)

where $\Delta\rho$ (density) and ΔU ($velocity$) are the differences between their values within the mixed layer, and their values below the mixed layer, respectively (Price et al., 1986). The variable ρ_0 is the reference density and g is the gravitational acceleration. Then, the model adds local shear instability below the mixed layer, where mixing due to strong shear is parameterized based on a threshold gradient Richardson number, R_{ig}, defined as: $R_{ig} = \frac{N^2}{S^2} = 0.25$ (2a)

where, S^2 is the square of the shear below the mixed layer and $N^2 = \frac{g}{\rho}\frac{\Delta\rho}{\Delta z}$ (2b)

The vertical resolution of the model depth bin was set to 2 meters to be aligned with the gridded glider data. The momentum (horizontal diffusivity) and vertical diffusivity were set to 10^{-5} m^2/s and 0 m^2/s, respectively (Sanikommu et al, 2020; Zhai et al., 2015). The maximum depth of the PWP experiment for the run and the initial depth range for the profiles of salinity and temperature were 400 m, the depth at which the divergence of hydrographic variables between summer and winter was minimal.

Estimation of the MLD at each time step throughout the PWP model run used the same criteria used for the glider data by determining the depth range over which the density increase relative to 10 m was no more than 0.03 kg/m^3 (de Boyer et al., 2004).

3 Results

3.1 Atmospheric forcing

Regional atmospheric forcing is a major factor affecting the seasonal variability of the Red Sea circulation. The wind direction in the northern Red Sea is predominantly from the north-northwest (NNW; Fig. 2a). The net heat flux was initially negative, with heat flux losses of up to 300 w/m^2 in January, up to 250 w/m2 in February, and transitioning in late March from net negative to net positive, thus beginning the onset of the seasonal heating period (Fig. 2b).
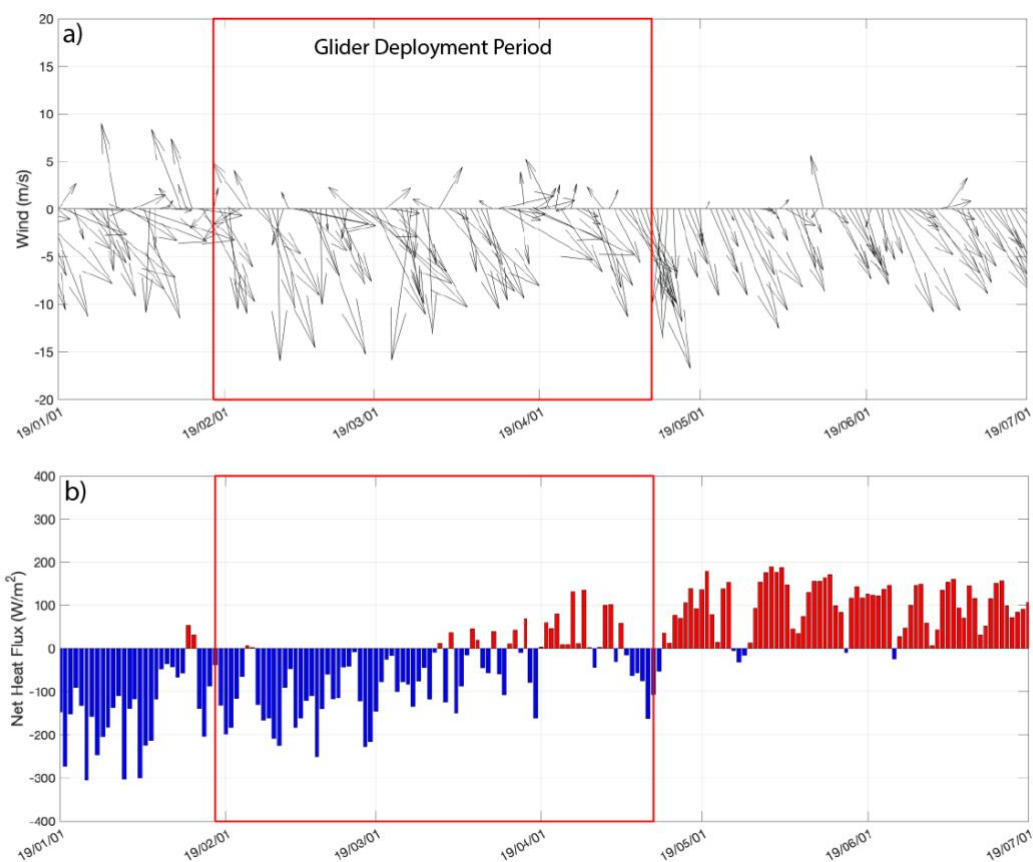
Figure 2: a) Wind vectors for the northern Red Sea and b) net heat flux for the northern Red Sea (average for the black dashed box over the NRS, Figure 1) for the period from January 1, 2019 through July 1, 2019. The red box indicates the period of the glider mission.

3.1 Upper ocean response to atmospheric forcing

3.1.1 Regional response from a remote sensing perspective

Remotely sensed ocean imagery demonstrates the seasonal evolution of the upper ocean during the glider deployment. Figure 3 provides images of 8-day composites for SLA and SLA-derived geostrophic velocity, sea surface temperature, and CHL concentration. At the onset of the glider deployment in late January–early February, the eastern boundary coastal flow was northward (Fig. 3a). Consistent with this northward flow, a tongue of warmer, low-CHL water extended northward along the Saudi coastline (Fig. 3b–c). These observations are consistent with previous observations from 2016 (Asfahani et al., 2020) and with the mean structure typically observed for SST in the winter months (Karnauskas and Jones, 2018). Cooler, higher

220 CHL water is observed on the western side of the basin, perhaps due to the convective mixing described by Kheireddine et al. (2020).
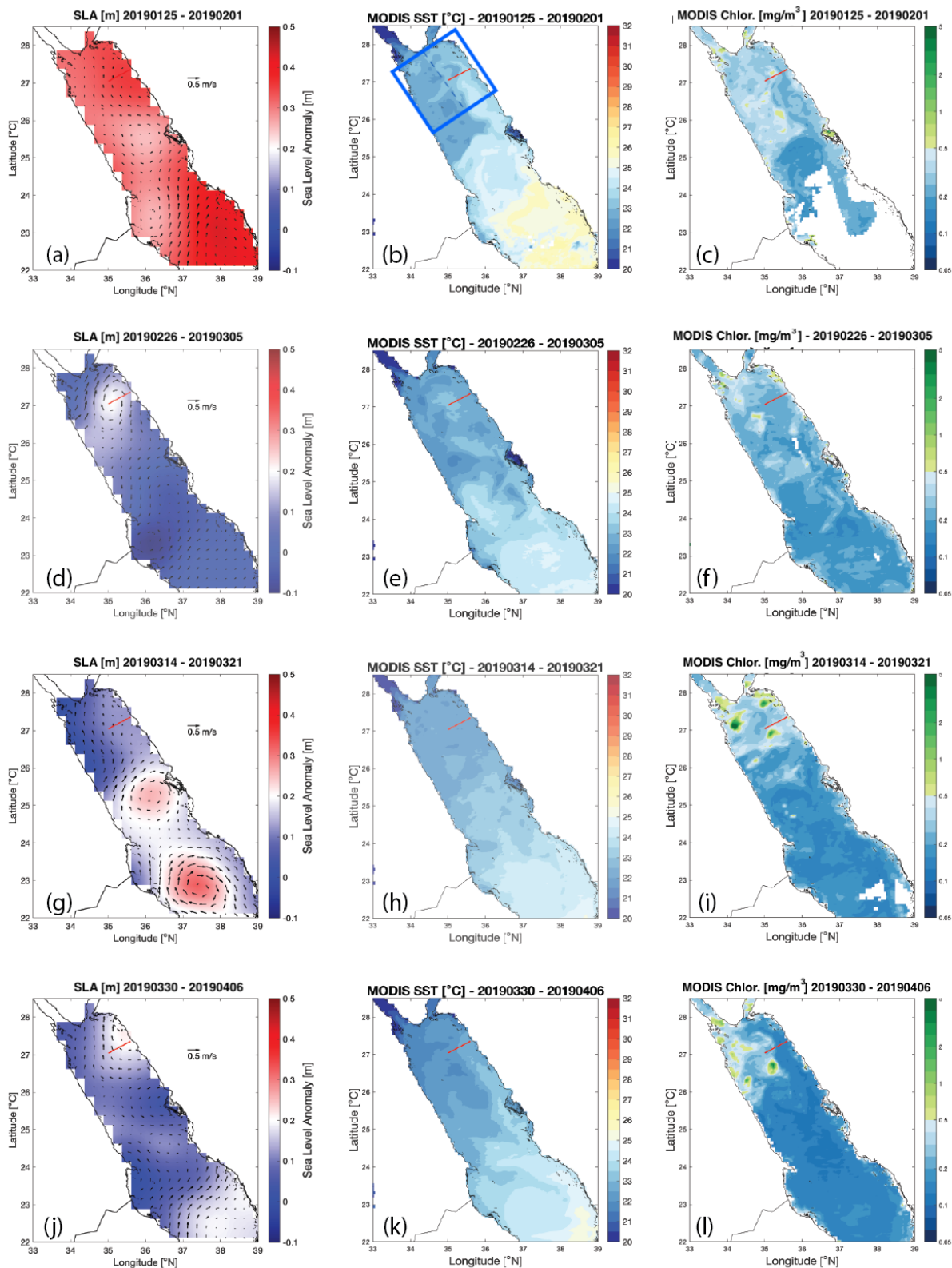
Figure 3: 8-day averages of sea level anomaly and geostrophic velocity (left-hand panels), 4 micron nighttime SST from the MODIS Aqua satellite (center panels), and CHL from MODIS OCI (right-hand panels) during the presence of the EBC (panels a-c), AE (panels d-f), pair of anticyclonic eddies (panels g-i), and lateral advection (panels j-l). The red line indicates the location of the Duba glider track. The blue box in panel b) indicates the region of the northern RS (NRS) that was used for regional averages (~ 200 km x 200 km). The dashed blue line divides the eastern half of the NRS from the western half.

Following the initial phase of northward coastal flow, an AE developed in the northeastern RS (Fig. 3d). During this period, the flow was southward across the glider line, and there was no indication of northward advection of warmer, low-CHL water (temperature > 24°C and CHL < 0.1 µmol/Kg) from the south (Fig. 3e-f). The AE appeared to block the warmer, low-CHL water transport into the region. The surface temperature of the NRS became cooler reaching a mean surface temperature near 22.5 °C and the temperature difference between the western and eastern sides of the northern region decreased to less than 0.25 °C (Fig. 3h and 4a).

In the latter half of March, two anticyclonic eddies (Fig. 3g), between 22 °N and 26 °N, apparently blocked the northward flow of water from the south and isolated the northern Red Sea from the inflow of the warmer, low-CHL water. Consequently, the near-surface in the NRS became almost thermally homogeneous, with small temperature variations in its spatial distribution (Fig. 3h). The densest surface water was observed in the NRS during this period (Fig. 4c). By the beginning of April, these two eddies had dissipated, and warm, low CHL water again advected into the NRS along the eastern coastline (Fig. 3j, 3k, and 3l), re-establishing the temperature differential between the eastern and western halves of the NRS (Fig. 4a-c).

3.1.2 Upper layer variability

As the atmosphere progressed through its typical annual cycle, the near surface ocean demonstrated high variability. In order to compare the data accurately, the depth of 6m has been chosen to represent the nearsurface layer, while the depth of 500 m has been selected because it is the most isolated from the surface influence and shows the least variability within the data set. The time series of surface (6 m) and 500 m values for temperature, salinity, and density are shown in Fig. 4. This is a continuous time series of glider data, irrespective of its location along the transect. Distinct phases are evident in the time series. The early phase, consistent with the atmospheric forcing, shows a general cooling trend from mixed layer temperatures near 24 °C in the early period to about 22.5 °C during the coolest phase, after which temperatures rose again to nearly 24 °C. For most of the period, the western half of the northern RS was cooler than the eastern half, where the glider was operating (Fig. 4a). However, during the coolest period, the temperatures were nearly homogeneous across the entire northern RS. Correspondingly, mixed layer salinities rose from values of 40–40.2 during the early phase to nearly 40.4 during the cool, salty period, then returned to values between 40 and 40.2 in the warming period. As a result, the near-surface density anomaly initially increased from 27.6-27.8 kg/m^3 to 28.3-28.4 kg/m^3 during the dense period. As expected, no effects of the surface forcing were apparent at 500 m.

In the latter part of the cooling phase (between February 17 and March 12), the MLD exceeded 100 m much of the time. Although the deepest mixed layer occurred during the cool, salty phase, the MLD during this period was highly variable (Fig.

4d). The variability in the MLD is a result of the new, well-formed cyclonic eddy during that time. Shallow MLD can be present in the center of a new-formed cyclonic eddy as is shown in Fig. 7 and it is also consistent with the patchiness of the

260   SST (Fig. 3e).
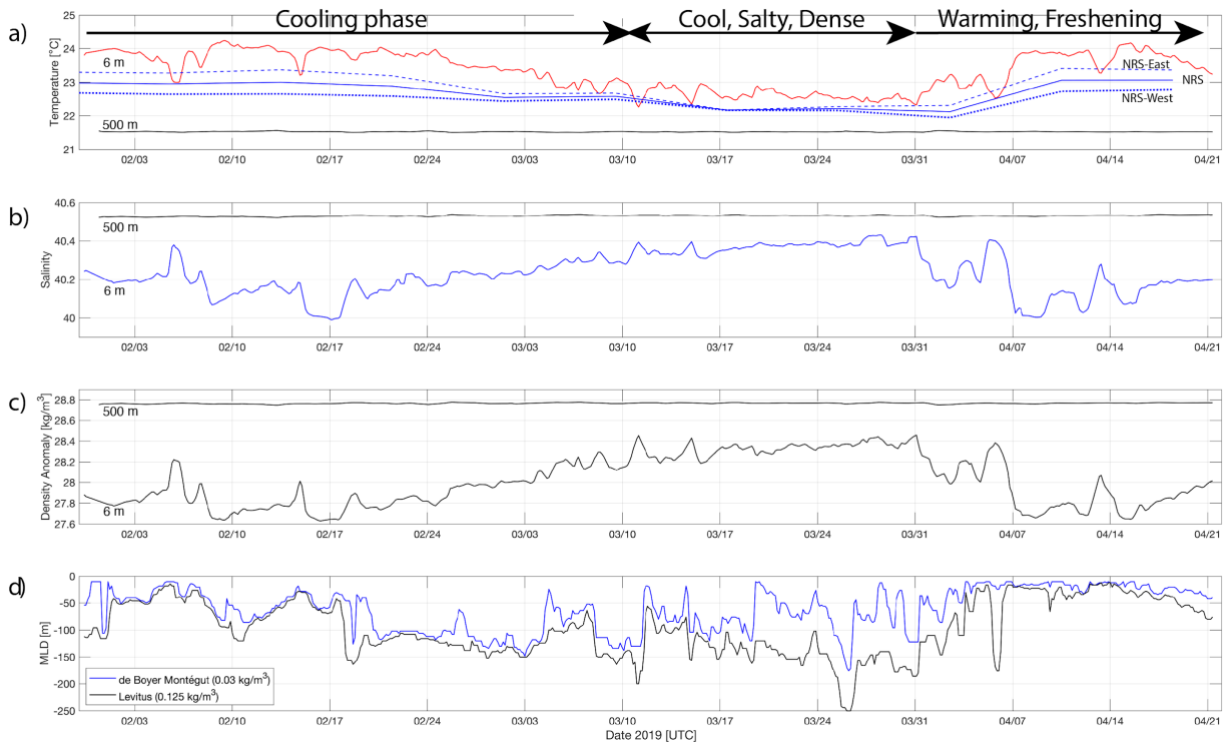
Figure 4: Time series of near-surface (6 m) and deep (500 m) temperature, salinity, density, and MLD for the glider deployment from January 31 through April 21, 2019. This is the complete time series, irrespective of the glider's location along the transect. In
265   **panel A, temperature averages from the 8-day MODIS SST are shown for the entire northern Red Sea (NRS, solid blue line), the eastern half of the northern Red Sea (NRS-East, dash blue line), and the western NRS (NRS-West, dotted blue line). The geographical boundaries of these subregions are shown in Figure 3b.**

Individual glider sections provide insight regarding mesoscale processes occurring in the NRS during this winter-spring period. In the early cooling phase, the isopycnals were tilted strongly downward from offshore to nearshore, with cool, dense water

270   near the surface offshore and warmer, fresher water near the surface nearshore (Fig. 5a and 5b). The overall geostrophic flow was northward, with an average velocity of 0.31 m/s in the upper 100 m (Fig. 5e), consistent with the geostrophic velocity calculated from the sea level anomaly (Fig. 3a). The maximum upper layer stratification occurred in the offshore 20 km of the transect where uplifting of the pycnocline resulted from the cyclonic circulation (Fig. 5d). The maximum near surface CHL concentration occurred where dense water (≥ 28.1 kg/m^3) offshore shallowed to within 50 m of the surface.

275   A small-scale cyclonic feature centered about 43 km offshore was embedded within the larger-scale flow (Fig. 5a, 5b, and 5e). This feature was not observed in either the previous or subsequent transect, each separated by approximately 3 days from the

current transect. Thus, it was a transient feature on the glider line which we conclude was advected across the glider line within the larger scale flow. A feature characterized by elevated CHL and dissolved oxygen, and low BVF extended to along the 28.2 kg/m^3 isopycnal between 20 and 40 km offshore. It spanned of depth range of about 150 m at 40 km offshore to 250 m at 20

280 km offshore, suggestive of subduction of denser near-surface water and downward transport along the isopycnal below the mixed layer and the euphotic zone (Fig 5c, 5d and 5f). We use the word subduction here as defined by Williams and Meijers (2019) - "the transfer of fluid from the mixed layer into the stratified pycnocline".
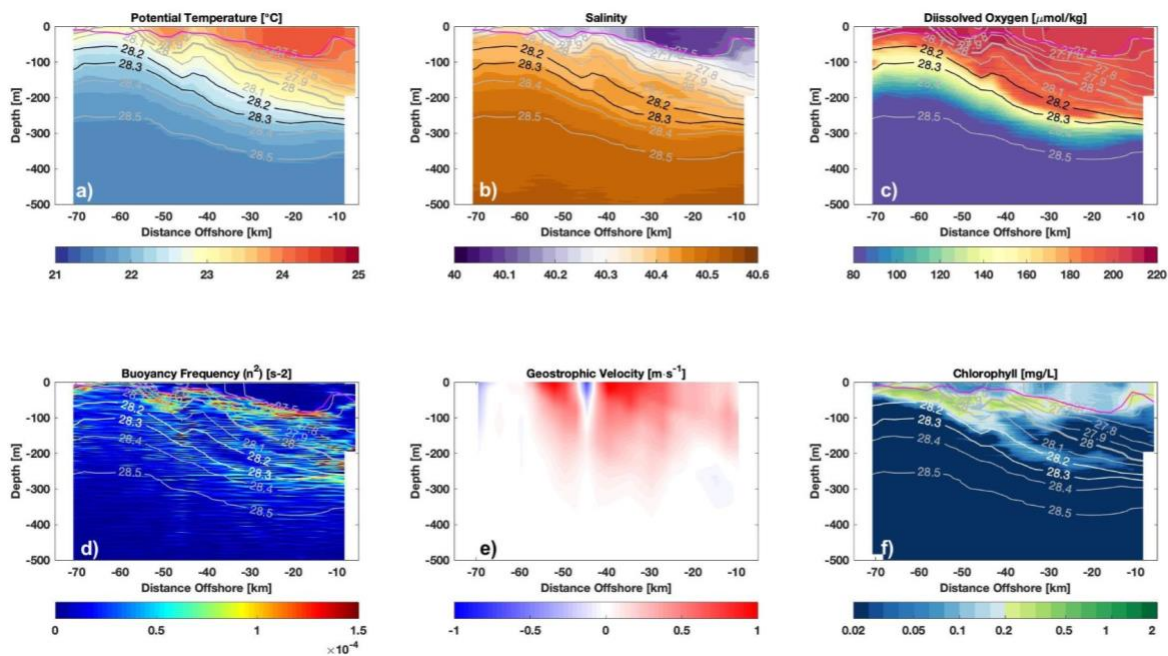
285 **Figure 5: Gridded glider section of a) Potential temperature, b) Salinity, c) Dissolved Oxygen, d) Brunt-Väisälä frequency, e) Geostrophic velocity, and f) Chlorophyll-a, for February 5–9, 2019. Density anomalies are shown in figures a, b, c, d, and f with solid green lines. The solid magenta line represents the MLD. Geostrophic velocity, calculated relative to 500 m, is positive to the north-northwest and negative to the south-southeast parallel with the coastline.**

290 Following the initial period of northward transport, the circulation changed significantly in late February, reversing the direction of flow across the glider line due to the presence of an AE in the north-eastern RS (Fig. 3d-f and 6). Based on glider sections, the southward coastal flow began in mid-February and persisted for approximately 3 weeks. The isopycnal structure associated with the anticyclonic geostrophic flow is evident below the mixed layer. In the glider section from March 1–5 the geostrophic velocity varied between weakly northward at the offshore and inshore ends of the line to a maximum southward

295 velocity of 0.67 m/s southward, and an average southward velocity of 0.14 m/s in the upper 100m, weaker in magnitude than the northward flow during the preceding cyclonic period (Fig. 6e). During this period, the upper boundary of the pycnocline,

28 kg/m³, which had been near the surface offshore during early February, was now at nearly 150 meters depth in the offshore portion of the transect but rose to the surface near the coast (Fig. 6a-b). The MLD was consistently deeper than 100 meters in the offshore 30 km of the transect, and in the near-shore 40 km, it varied between ~25 and 120 m. CHL was uniformly

300   distributed within the mixed layer with diel patterns in concentration, which appear as spatial patterns in the 3.5-day transit of the line (Fig. 6f). Oxygenated waters spread down to almost 120 m within the mixed layer (Fig. 6c). A bolus of highly oxygenated water was observed between the density surfaces of 28.2 and 28.4 kg/m³, between 20 and 50 km offshore, and in the depth range of 150 to 250 m. This water was slightly warmer (∼22.3°C) and higher in salinity (∼40.43) than in other regions along the transect within this isopycnal range, and stratification was weak (Fig. 6d). This bolus is likely to be outflow

305   water from the Gulfs of Aqaba or Suez that has advected into this region with the southward flow.
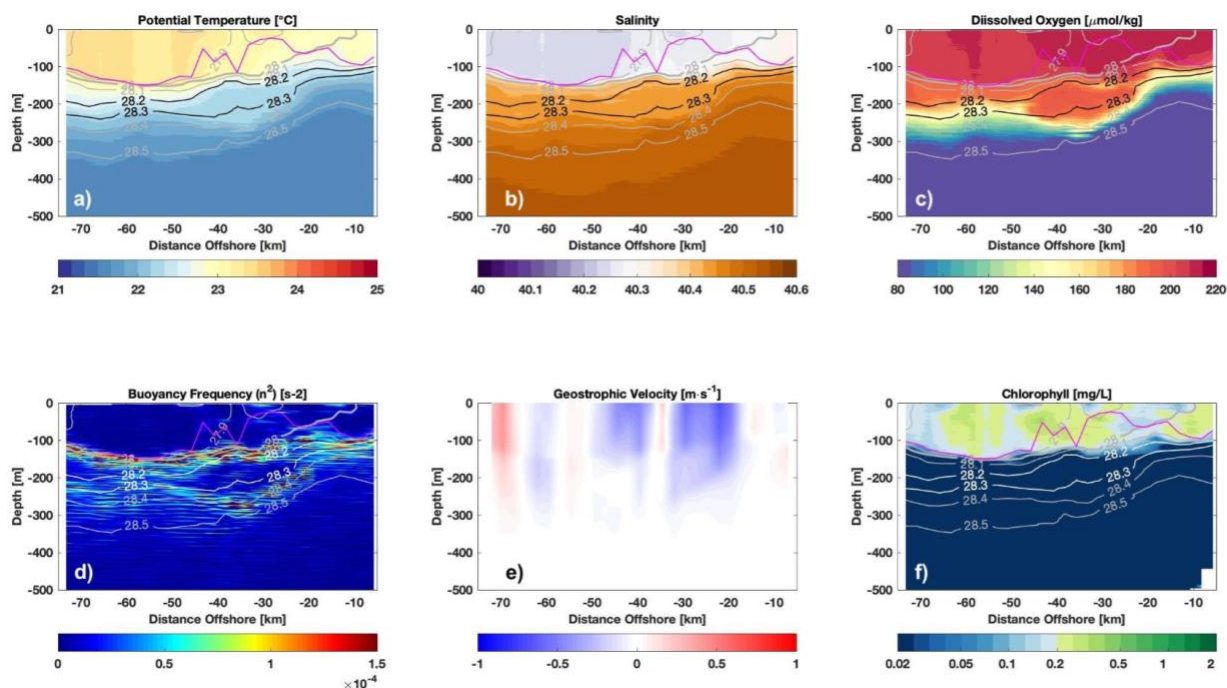
Figure 6: Same as for Figure 5, but for the period of March 1–5, 2019.

The near-surface temperature continued to decrease through March, while salinity increased within the surface layer, reaching

310   a maximum salinity of 40.4 and a density anomaly of about 28.4 kg/m³ in late March (Fig. 4). The corresponding glider section of temperature and salinity for this period (Fig. 7a-b), March 26–29, shows that the coolest, saltiest, and densest water occurred in the center of a cyclonic eddy about 40–45 km offshore, where the dense isopycnals (>28.2 kg/m³) outcrop at the surface. Across this transect, the near-surface temperature was less than 22.8 °C, the minimum salinity was more than 40.3, the minimum near-surface density was >28 kg/m³, and the minimum stratification was <1x10⁻⁴ (Fig. 7d). Prior to this, the

315 shallowest that the 28.2 kg/m³ isopycnal was observed was in the early section between February 5 and 9, at a depth of about 90 m at the offshore end of the transect. In the same transect, the isopycnal descended below 250 m nearshore. Mixed layer depth along this transect ranged from as shallow as 12 m to as deep as 148 m on the inshore end of the transect, on the periphery of the eddy circulation. In the eddy center, the mixed layer extended to the depth of the 28.3 kg/m³ isopycnal where stratification due to the uplifted pycnocline impeded deeper mixing. The isopycnal uplifting appears to be in the center of a

320 cyclonic feature where the geostrophic velocity (Fig. 7e) is northward nearshore (0.5 m/s) and southward offshore (0.2 m/s) As in earlier sections, small-scale structures are apparent and potentially important to biogeochemical processes. At about 20 km offshore, a low DO and low CHL feature extends upward from about 200 m to at least 100 m depth (Fig. 7c and 7f). The low DO concentration extends to shallower depths. The presence of the CE leads to an uplift of the isopycnals about 50 km offshore (Fig. 7). In the shoreward periphery of this eddy (~20 km offshore), both CHL and DO penetrate to a depth of up to

325 250m, well below the mixed layer and euphotic zone depth (Fig. 7c and 7f). This subduction occurs near the nearshore reversal of flow.
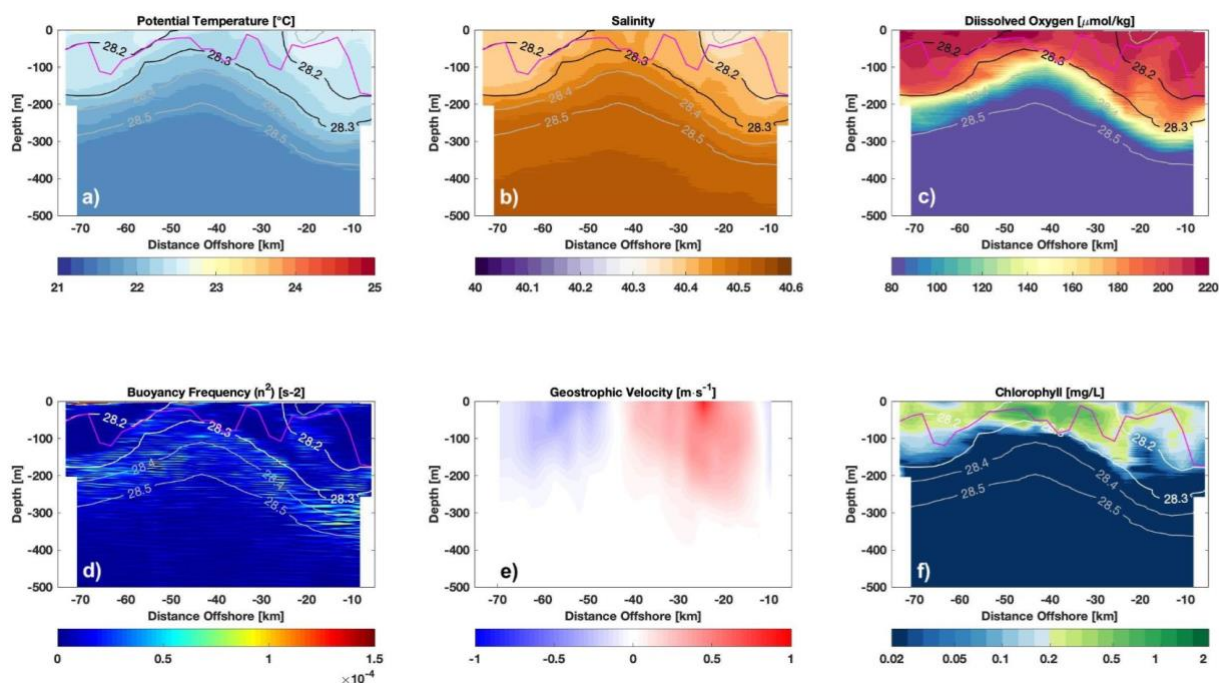
330 **Figure 7: Same as for Figure 5, but for the period of March 26–29, 2019.**

Immediately following this cool period, warmer, fresher water began to appear in the nearshore region of the glider line (Fig. 8a and 8b). The shallowing of lower-oxygen water, hence nutrient-rich, offshore between 35 and 50 km was observed in late

March and subsided with the weakening of the cyclonic circulation (Fig. 8c). The cyclonic circulation remained, but it was entraining the warmer, fresher water from the southward, as is evident in the composite SST image from March 30-April 6

335 (Fig. 3k). This warming and freshening continued through the remainder of the glider deployment (Fig. 4a). Freshening was evident on the nearshore half of the glider line, where salinities fell below 40.3, while remaining higher along the offshore half of the line. Denser water subsided except at the outer half of the transect. Although the direction of the geostrophic velocity was similar in pattern to the previous period (Fig. 7e), the magnitude of the nearshore flow intensified by 0.2 m/s, while the offshore flow was similar to the previous transect (Fig. 8e). Figure 8f shows that the CHL concentration between 35 and 50

340 km offshore decreased as warmer water was entrained near the coast.

Subduction is also present between 30 and 10 km onshore and is clearly observed in the BVF panel and in CHL and DO (Fig. 8c, 8d and 8f). The subduction displaces the pigments of CHL and DO deeper than 200 m nearshore; in the offshore area, these two parameters are well distributed in the first 100 m.
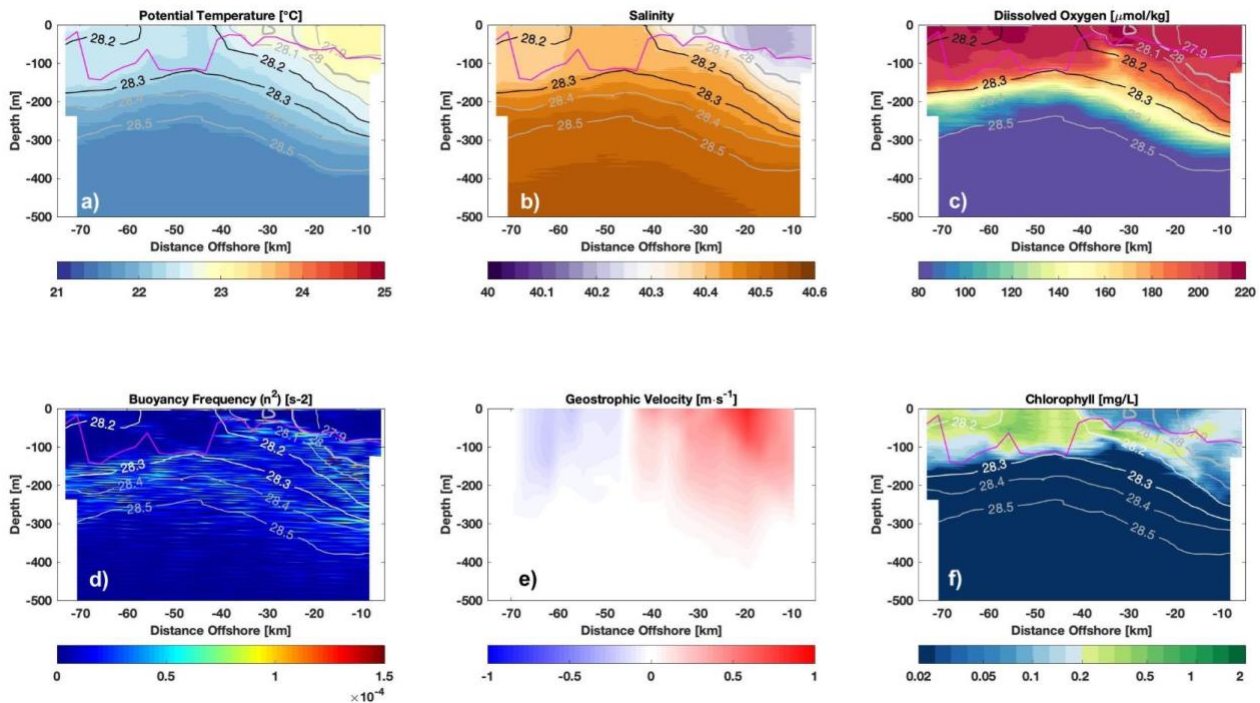
345

Figure 8: Same as for Figure 5, but for the period of March 29-April 2, 2019.

4 Discussion

350   The Northern Red Sea, influenced by strong atmospheric forcing, completes the conditioning of the upper ocean for dense water formation. Both modelling and some limited observational studies have demonstrated that cyclonic eddies, wintertime cooling, and deep convection contribute to RSOW formation (Asfahani et al., 2020; Sofianos and Johns, 2003; Papadopoulos et al., 2015).

Unlike previous observations and interpretations of the NRS (e.g., Asfahani et al., 2020; Papadopoulos et al., 2015; Yao and
355   Hoteit, 2018), a reversal of the currents in the eastern half of the basin prevented the inflow of warmer, fresher water from the south. During this phase, the upper layer of the NRS became relatively homogeneous, and near-surface water along the glider line reached its maximum salinities and densities (Fig. 5a and 7a).

To evaluate the similarities and differences with previous years, an EOF analysis was performed on the SLA data between 26 ˚N and 28 ˚N over a period of 4 years that has been considered efficient (from 2016 to 2019; Fig. 9). The first mode of the
360   EOF describes 86.6 % of the SLA variation (Fig. 9a). In the years 2016–2018, the EOF of the SLA showed a relatively positive or neutral pattern during the winter-spring transition period, which continued until May, when the EOFs typically decreased (Fig. 9b). This late spring decrease generally coincides with the transition from a net negative air-sea heat flux to a net positive flux (see Fig. 2b). For 2019, the first mode of the EOF showed a distinct increase in late January through mid-February, then became negative through mid-March, in contrast to the pattern in previous years. This negative phase is consistent with the
365   period when the circulation was anticyclonic. The flow of warmer, fresher water from the south was apparently blocked during this period, and the temperature became relatively homogeneous in the NRS.
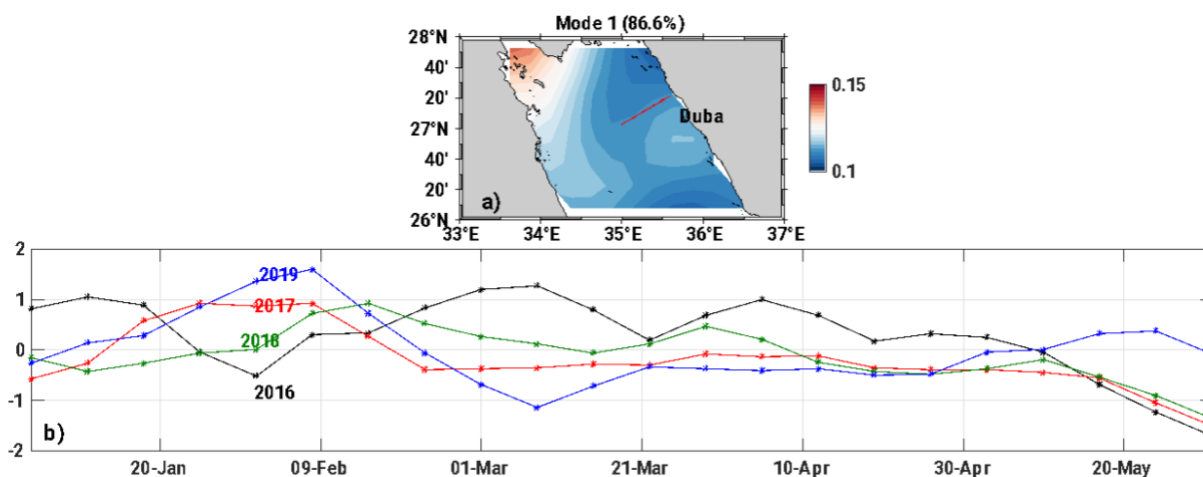
370   **Figure 9: The first mode of the EOF based on the SLA weekly mean in 2019. (a) the spatial pattern of the first mode. (b) time series graph of the first mode for four (4) subsequent years: 2016 (black), 2017 (red), 2018 (green), and 2019 (blue) from January to May.**

We examined the relationship between the first mode of the EOF and atmospheric forcing using a time-lagged correlation. No clear correlation was discernible from this analysis (not shown). But in comparison with the previously published observations from 2016 (Asfahani et al., 2020*)*, the period of negative average heat flux lasted longer into the spring. Thus, there is an

375 overall difference in the duration of the negative heat flux between the 2016 observations and the observations in 2019.

The surface layers responded to the heat loss with decreased temperatures and increased salinity and density. The cumulative effect of the cooling through the entire winter period resulted in the formation of the densest surface waters in late March, when the difference in temperature and salinity between the surface and the deep layers was at a minimum. Following this cooling phase, the net heat flux fluctuated around zero. Then in early April, the weakening of the atmospheric forcing, the

380 transition to positive heat fluxes, and restratification due to advection from the south resulted in a near-surface temperature increase of 1°C and a salinity decrease of 0.2, both of which contributed to the near-surface density decrease in April (Fig. 4). The warmer, less saline, and thus lighter water from the south spread into the area, and during the restratification, it overrode the denser waters, isolating them from additional direct ocean-atmospheric interaction.

The water underlying the more buoyant surface water, which lies along the 28.2 kg/m^3 isopycnal, extended from the surface

385 in mid-transect to approximately 200m nearest the coast (Fig. 8). This recently exposed subsurface water spreads in the basin, and its signal can be detected in the CRS, as mentioned by Zarokanellos and Jones (2021). This water results from the northward advection of GASW, which is subjected to evaporation along its entire transit of the Red Sea. Winter cooling throughout the entire period further modifies the transported surface water in the NRS. During this particular year, the presence of the AE in the NRS temporarily blocked advection from the south, contributing to the surface waters' extended exposure to

390 the atmosphere. Near the end of the cooling period, when the surface water reached its maximum density, the cyclonic circulation was reestablished, contributing to the inflow of buoyant GASW which overlaid the denser water.

In this study, the PWP model was applied to subsets of the observational period to further understand the relationship between the local heat flux and the advection of water from the south. The model used daily surface heat flux and wind stress as a pronounced diurnal cycle was not apparent in the observed salinity and temperature data. Of course, this simple 1-dimensional

395 model will not capture the spatial variability both in the water column structure and in the atmospheric forcing field, but it demonstrates how the atmospheric forcing would drive the seasonal evolution of the mixed layer without these complicating factors. Krokos et al. (2022) used a 4-dimensional MIT-GCM model to analyze the spatial and seasonal evolution of mixed layer variability in the entire Red Sea demonstrating the importance of atmospheric forcing especially through the influence of mixed layer temperature.

400 Figure 10 shows the evolution of the MLD in the upper 200 m based on the PWP simulation. Three separate PWP simulations were performed, initiating each simulation at the onset of one of the three phases determined from the in-situ observations. he initial temperature and salinity profiles for the model run were taken from the glider section nearest the initiation point of the run. The cooling phase extended from February 1st until March 8th (35 days). During this period, first presence of a mesoscale cyclonic eddy and later an anticyclonic eddy in the study area were observed. In the same period, the simulated MLD is

405 constantly deepening, reaching a maximum depth of 162m at the end of the cooling phase.

During the dense phase, the observed MLD shows large fluctuations and mismatches with the simulated MLD. The 1-D model failed to capture the shallowing of MLD during the dense phase. The observed discrepancy is based on the pycnocline depth that shallowed substantially, such that the dense pycnocline intersected with the surface. Lastly, the PWP-simulated MLD during the warming phase also shows a discrepancy with the observed MLD. During this phase, the observed MLD rapidly

410   shallowed to less than 45 m, and the mean MLD was about 20 m. The shallowing of the MLD during the warming and freshening phases was attributed, in part, to the northward flux of the buoyant Gulf of Aden Water. But the shallowing of the pycnocline due to the cyclonic eddy also contributed to the shallowing of the ML, as seen clearly in Fig. 8.
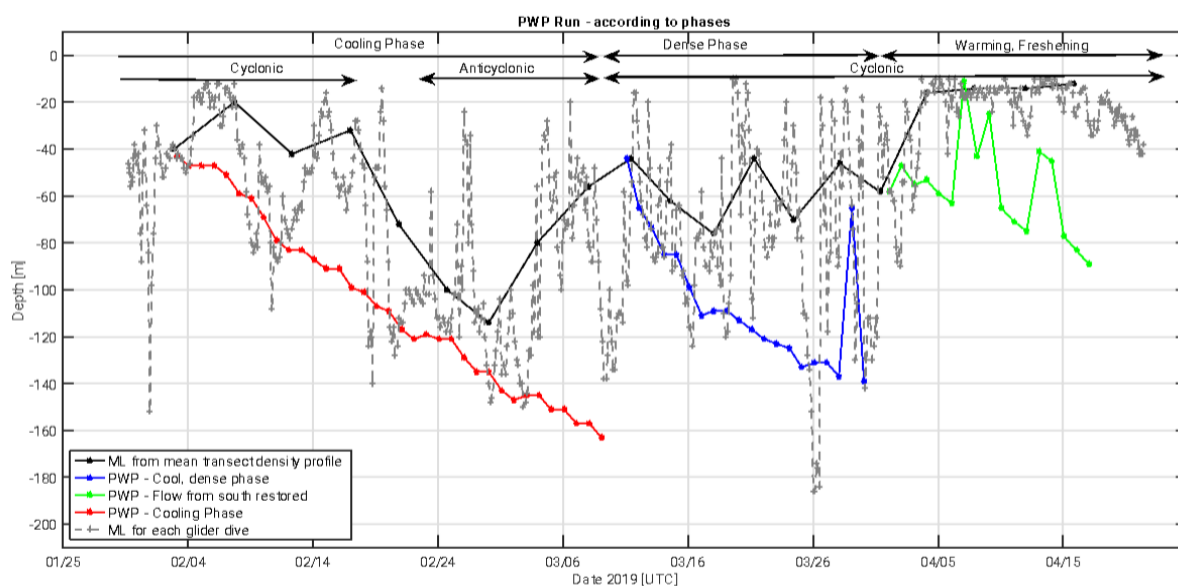
415

Figure 10: Comparison between the observed transect-averaged MLD from the glider (black) and PWP-simulated MLD during the 1) cooling phase (red), 2) cool-salty and dense phase (blue), and 3) warming- - freshening phase (green). The black + symbol shows the MLD for each dive, interconnected by the black dashed line.

420   Water mass subduction is a component of the formation of Red Sea Outflow Water during winter and a contributor to the vertical carbon flux from the euphotic layer to the interior of the Red Sea. As shown in Fig. 5, a water mass containing elevated chlorophyll and oxygen can extend well below the mixed layer and euphotic zone. Although only one example with this feature (February 5-9, Fig. 5) is shown in this paper., subducted water was evident in the glider deployment from its deployment on January 30 through the fourth transect that was completed on February 18. Key characteristics of this feature were elevated

425   chlorophyll and dissolved oxygen on the 28.2 kg/m^3 isopycnal that extended to as deep as 250 meters. In Fig. 5, this feature was evident from about 45 km offshore and shoreward. Fig. 11 shows the relationship between these variables and density

between 20 and 40 km offshore. A clear peak in both variables aligns with the 28.2 kg/m^3 isopycnal. Inshore, at 45 km, the region between 150 and 500 m contains a measurable fraction of the total chlorophyll.

Given the limitations of our observations, constrained by the Exclusive Economic Zone (EEZ) boundary, the full mechanism
430 of the formation of this subducted layer is unclear. One possible mechanism is that either vertical mixing or sinking of particles on the western half of the northern Red Sea (Kheireddine et al., 2020) could create this feature, which is then entrained into the cyclonic circulation in this region and transported from the western side of the basin to the eastern side. Regardless of the details of the mechanism, subduction is a process that needs to be considered in the physical and biogeochemical dynamics of the northern Red Sea.

435
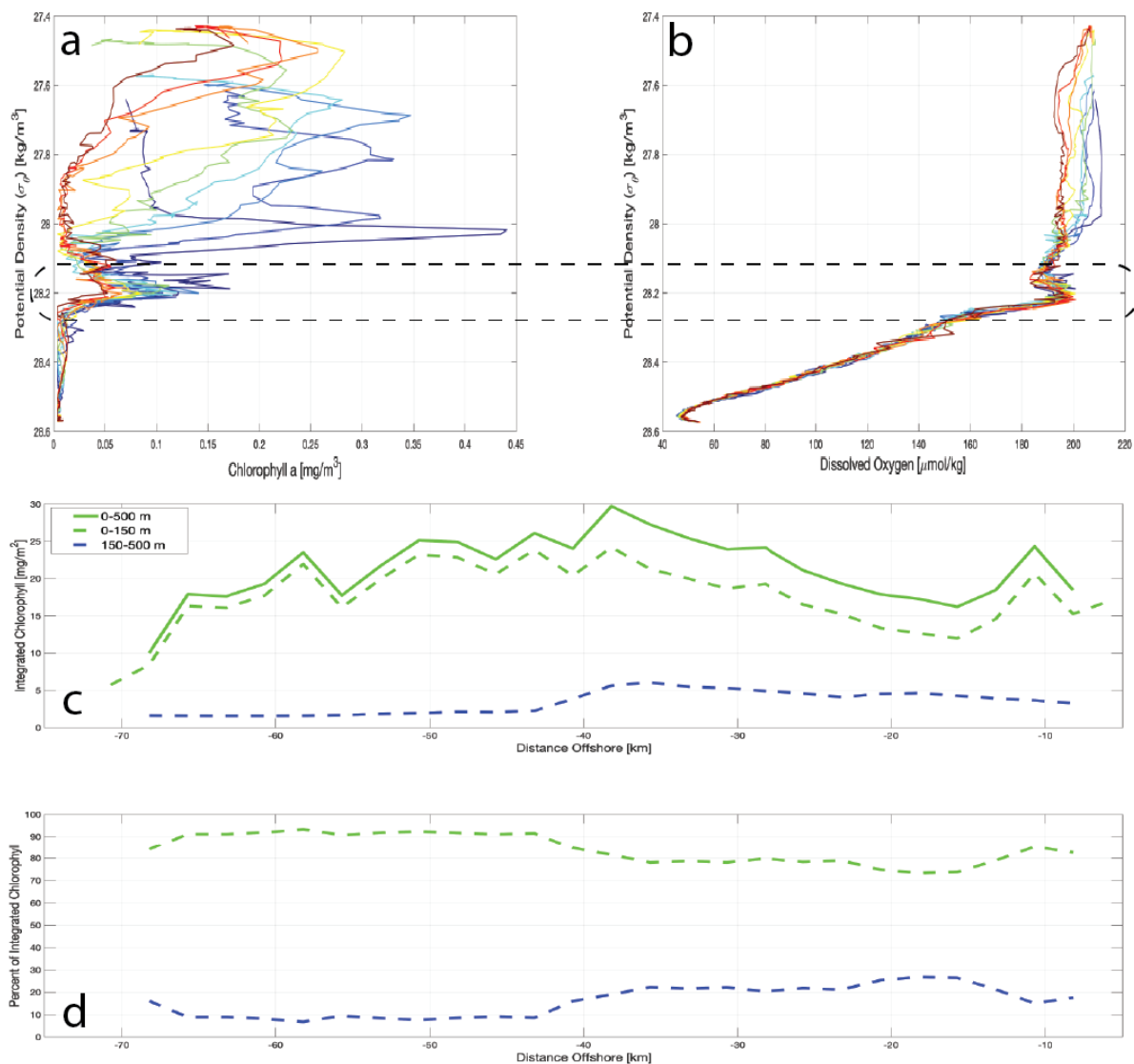
Figure 11: Characteristics of the subducted feature in transect 2, February 4–9 (Figure 5). Panels a and b show the concentrations of chlorophyll and dissolved oxygen as a function of density for profiles between 20 and 40 km offshore. Panel c shows the integrated chlorophyll as a function of distance offshore. The solid green line is the total integrated chlorophyll between the surface and 500 meters. The dashed green line is the integrated chlorophyll between the surface and 150 m, and the blue line is the integrated chlorophyll between 150 and 500 m. Panel d shows these concentrations as a percentage of the total integrated chlorophyll.

440

5 Conclusion

445 The mechanism of the RSOW formation in the NRS is well connected with the presence of the cyclonic eddy and the strong winter cooling, as has been described by previous studies (Asfahani et al. (2020), Sofianos and Johns (2003), Papadopoulos et al. (2015), Yao et al. (2014b)). Water mass subduction is a contributor to RSOW formation that has not been previously discussed, although its relative contribution has not been estimated. Moreover, the transition from negative heat flux to positive heat flux and the re-establishment of the northward flow of the water along the eastern coast of the Red Sea foretell the ending

450 of the RSOW formation as the less dense water from the south caps the denser northern Red Sea water terminating the exposure of denser water to the atmosphere. Subduction contributes to the downward flux of carbon, as indicated by the presence of CHL, from the surface to deeper layers well below the euphotic zone and the ventilation of the subsurface region, as indicated by the elevated DO along the 28.2 $kg \cdot m^{-3}$ isopycnal. We observed an eddy reversal in the region south of the study area that prevented the advection of the more buoyant surface water into the area. We were not able to explain the mechanism for the

455 observed eddy reversal from our observations and 1D model simulations. Papadopoulos et al. (2015) discuss the contribution of the outflow from the two northern Gulfs to deep water formation, but as a result of the temporary anticyclonic circulation, we see in these observations the presence of a water mass that likely originated from one of the gulfs in the depth and density range of Red Sea outflow water. Thus, this data set shows the contribution of multiple factors to the formation of Red Sea outflow water in the northern Red Sea that include surfacing of dense isopycnals due to the cyclonic circulation, significant

460 vertical mixing, dense outflow from the northern gulfs, water mass subduction, extension of the period exposure of dense isopycnals to the atmosphere due to blockage of the buoyant flux from the south, and termination of these processes with the reestablishment of the cyclonic circulation and the buoyancy flux from the south. In addition, it is clear that submesoscale features are present in the region and contribute to the overall physical and biogeochemical dynamics of the region. What is clear in this data set is that multiple processes that have not been previously combined contribute to the formation of Red Sea

465 Outflow Water and to biogeochemical fluxes in the northern Red Sea (Table 2). In the future, it would be invaluable to have a combined detailed observational and modelling study using multiple autonomous platforms and ship-based sampling spanning the entire northern Red Sea basin to full depth. This would resolve the 4-dimensional variability within the basin and provide insights into the sources and sinks in the process of the formation of the outflow water.

470

Contributing Mechanisms	Yao et al 2014 (a & b)	Papadopoulos et al 2015	Asfahani et al 2021	Krokos et al 2022	This Study
Cyclonic Circulation leading to exposure of dense isopycnals	√	√	√		√
Convective mixing	√	√	√	√	√
Upwelling/Downwelling along boundaries	√				
Outflow from Gulfs		√			√
Along basin pressure gradients	√				
Submesososcale processes					√
Subduction of dense water from surface water into pycnocline					√
Anticyclonic blockage of northward flow of buoyant water into NRS					√
Biogeochemical effects					
Eddy driven upwelling nutrient flux		√	√		√
Convective mixing nutrient flux into euphotic zone			√		√
Subduction results in the downward transport of dissolved oxygen and particulate carbon below the euphotic zone					√

Table 2: Summary of the major conclusions from the related studies relative to the formation of the RSOW in NRS.

Data availability

475 The data sets that are presented in this paper (glider time series and gridded sections, 8-day remotely sensed SST, chlorophyll, and sea level anomaly/geostrophic velocity, and the NASA MERRA-2 reanalysis data) are available through the Zenodo repository (https://doi.org/10.5281/zenodo.11046900) https://zenodo.org/records/11046900?preview=1&token=eyJhbGciOiJIUzUxMiJ9.eyJpZCI6IjA4ZDdkMzY0LTQyMGUtNGRiYS

Author contribution:

All authors have contributed to Conceptualization, Data Curation, Formal Analysis, Investigation, Writing – original draft preparation and Writing – review & editing**.** Visualization is done by L.E., Z.K. and B.H.J.. Software is done by L.E. and
485 B.H.J.. while supervision is done by Z.K. and B.H.J..

Competing interests

The authors declare that they have no conflict of interest.

490 **Acknowledgements**

The authors gratefully acknowledge the NASA Goddard Space Flight Center, Ocean Ecology Laboratory, Ocean Biology Processing Group for remote sensing data and the Copernicus website for the SLA data used in this study. The authors are grateful to the KAUST Coastal Marine Resources Core Lab (CMRCL) for their engineering and field support during the glider operations. Particular thanks go to Thomas Hoover, Samer Mahmoud, Mohammed A. Aljahdli and Lloyd Smith for their help
495 with the glider deployments. The authors also are grateful to Dr. Luc Rainville for his suggestions and discussions regarding the PWP implementation. Funding from King Abdullah University of Science and Technology (KAUST) supported the research in this publication. The ocean color products were obtained from NASA Ocean Color Group. The data are freely available online through the official website https://oceandata.sci.gsfc.nasa.gov/directdataaccess/Level-3%20Mapped/Aqua-MODIS/2019/. The altimeter products were produced by Ssalto/Duacs and distributed by Aviso+, with support from Cnes
500 (https://www.aviso.altimetry.fr). Dataset accessed [2022-01-27] at 10.5067/MODAM-8D4N9. The SST data source is NASA OBPG. 2020. MODIS Aqua Global Level 3 Mapped SST. Ver. 2019.0. PO.DAAC, CA, USA. MODIS CHL level 3 data was obtained via https://oceancolor.gsfc.nasa.gov/cgi/l3. We would like to acknowledge that the author Z.K. was partially part of the ITINERIS project.

505 **Financial support**

We thank the EU—Next Generation EU Mission 4 "Education and Research"—Component 2: "From research to business"—Investment 3.1: "Fund for the realisation of an integrated system of research and innovation infrastructures"—Project IR0000032—ITINERIS—Italian Integrated Environmental Research Infrastructures System—CUP B53C22002150006 for partially funding the author Z.K.

510

References

Abualnaja, Y., V. P. Papadopoulos, S. a. Josey, I. Hoteit, H. Kontoyiannis, and D. E.: Raitsos Impacts of Climate Modes on Air-Sea Heat Exchange in the Red Sea, Journal of Climate, 28(7), 2665–2681, doi: 10.1175/JCLI-D-14-00379.1, 2015.

Asfahani, K., G. Krokos, V. P. Papadopoulos, B. H. Jones, S. Sofianos, M. Kheireddine, and I. Hoteit: Capturing a Mode of

515 Intermediate Water Formation in the Red Sea, Journal of Geophysical Research: Oceans, 125(4), e2019JC015803, https://doi.org/10.1029/2019jc015803, 2020.

Beal, L. M., A. Ffield, and A. L. Gordon: Spreading of Red Sea overflow waters in the Indian Ocean, Journal of Geophysical Research, 105(C4), 8549–8564, doi:10.1029/1999JC900306, 2000.

Biton, H. Gildor, and W. R. Peltier: Red Sea during the Last Glacial Maximum: Implications for sea level reconstruction,

520 Paleoceanography, 23, PA1214.doi:10.1029/2007PA001431, 2008.

Biton, Gildor, Trommer, Siccha, Kucera, van der Meer, and Schouten: Sensitivity of Red Sea circulation to monsoonal variability during the Holocene: An integrated data and modelling study, Paleoceanography, 25(PA4209), 1-16, doi:10.1029/2009PA001876, 2010.

Bower, A. S., and J. T. Farrar: Air-Sea Interaction and Horizontal Circulation in the Red Sea, in The Red Sea, edited by N. M.

525 A. Rasul and I. C. F. Stewart, pp. 329-342, doi:10.1007/978-3-662-45201-1_19, 2015.

Bower, A. S., and H. H. Furey: Mesoscale eddies in the Gulf of Aden and their impact on the spreading of Red Sea Outflow Water, Progress in Oceanography, 96(1), 14-39, doi:10.1016/j.pocean.2011.09.003, 2010.

Cember, R. P.: On the sources, formation, and circulation of Red Sea deep water, Journal of Geophysical Research: Oceans, 93(C7), 8175-8191, doi:10.1029/JC093iC07p08175,1988.

530 Chen, C., Li, R., Pratt, L., Limeburner, R., Beardsley, R. C., Bower, A., Jiang, H., Abualnaja, Y., Xu, Q., Lin, H., Liu, X., Lan, J., & Kim, T.: Process modeling studies of physical mechanisms of the formation of an anticyclonic eddy in the central Red Sea, Journal of Geophysical Research: Oceans, 119, 1445–1464. doi:10.1002/2013JC00935, 2014

Churchill, J. H., Lentz, S. J., Farrar, J. T., Abualnaja, Y.: Properties of Red Sea coastal currents, Continental Shelf Research, 78, 51–61.doi:10.1016/j.csr.2014.01.025, 2014.

535 Clifford, M., C. Horton, J. Schmitz, and L. H. Kantha: An oceanographic nowcast/forecast system for the Red Sea, Journal of Geophysical Research, 102(C11), 25,101-125,112. doi: 10.1029/97JC01919, 1997.

de Boyer Montegùt, C., G. Madec, A. S. Fischer, A. Lazar, and D. Iudicon: Mixed layer depth over the global ocean: An examination of profile data and a profile-based climatology, Journal of Geophysical Research, 109(C12003), doi:10.1029/2004JC002378, 2004.

540 Edwards, A. J., and S. M. Head: Red Sea, Key Environments Series, Pergamon Press, Oxford, doi:10.1016/B978-0-08-028873-4.50008-6, 1987.

Emery, W. J.: Water types and water masses, in Encyclopedia of ocean sciences, edited, pp. 3179-3187, Elsevier, doi: 10.1006/rwos.2001.0108, 2001.

Eshel, M. A. Cane, and M. B. Blumenthal: Modes of subsurface, intermediate and deep-water renewal in the Red-Sea, Journal of Geophysical Research: Oceans, 99(C8), 15941-15952. doi: 10.1029/94JC01131, 1994.

Eshel, and N. H. Naik: Climatological Coastal Jet Collision, Intermediate Water Formation, and the General Circulation of the Red Sea, Journal of Physical Oceanography, 27, 1233-1257. doi: 10.1175/1520-0485(1997)027<1233:CCJCIW>2.0.CO;2, 1997.

Eyouni, L., Kokkini, Z., Zarokanellos, N., & Jones, B.. Mechanisms of the Overturning Circulation in the Northern Red Sea [Data set]. Zenodo. https://doi.org/10.5281/zenodo.11046900, 2024.

Fairall, C.W., E.F. Bradley, D.P. Rogers, J.B. Edson, G.S. Young: Bulk parameterization of air-sea fluxes for tropical ocean-global atmosphere coupled-ocean atmosphere response experiment, J. Geophys. Res. 101 (C2) 3747–3764 doi: 10.1029/95JC03205, 1996.

Garcia H. E., K.W. Weathers, C.R. Paver, I. Smolyar, T.P. Boyer, R.A. Locarnini, M.M. Zweng, A.V. Mishonov, O.K. Baranova, D. Seidov, and J.R. Reagan: World Ocean Atlas 2018, Volume 3: Dissolved Oxygen, Apparent Oxygen Utilization, and Dissolved Oxygen Saturation. A. Mishonov Technical Editor. NOAA Atlas NESDIS 83, 38pp, 2019.

GEBCO Bathymetric Compilation Group 2021: The GEBCO_2021 Grid - a continuous terrain model of the global oceans and land. NERC EDS British Oceanographic Data Centre NOC. doi:10.5285/c6612cbe-50b3-0cff-e053-6c86abc09f8f, 2021.

Gelaro, R., McCarty, W., Suárez, M. J., Todling, R., Molod, A., Takacs, L., Randles, C. A., Darmenov, A., Bosilovich, M. G., Reichle, R., Wargan, K., Coy, L., Cullather, R., Draper, C., Akella, S., Buchard, V., Conaty, A., da Silva, A. M., Gu, W., Kim, G.-K., Koster, R., Lucchesi, R., Merkova, D., Nielsen, J. E., Partyka, G., Pawson, S., Putman, W., Rienecker, M., Schubert, S. D., Sienkiewicz, M., & Zhao, B.: The Modern-Era Retrospective Analysis for Research and Applications, Version 2 (MERRA-2), *Journal Of Climate*, *30*, 5419-5454, 2017.

Iselin, C. O. D.: The influence of vertical and lateral turbulence on the characteristics of the waters at mid-depths, Eos, Transactions American Geophysical Union, 20(3). doi 10.1029/TR020i003p00414, 1939.

Jain, V., Shankar, D., Vinayachandran, P.N. et al.: Evidence for the existence of Persian Gulf Water and Red Sea Water in the Bay of Bengal. Clim Dyn **48,** 3207–3226. doi: 10.1007/s00382-016-3259-4, 2017

Johnson, K. S., J. N. J. N. Plant, S. C. Riser, and D. Gilbert: Air Oxygen Calibration of Oxygen Optodes on a Profiling Float Array, Journal of Atmospheric and Oceanic Technology, 2160–2172. doi 10.1175/JTECH-D-15-0101.1, 2015

Karnauskas, K. B., and B. H. Jones: The Interannual Variability of Sea Surface Temperature in the Red Sea From 35 Years of Satellite and In Situ Observations, Journal of Geophysical Research: Oceans, 123(8), 5824-5841, doi: 10.1029/2017JC013320, 2018.

Kheireddine, M., Dall'Olmo, G., Ouhssain, M., Krokos, G., Claustre, H.,Schmechtig, C., et al.: Organic carbon export and loss rates in the RedSea.Global Biogeochemical Cycles,34,e2020GB006650. doi:10.1029/2020GB006650, 2020

575 Krokos, G., Cerovečki, I., Papadopoulos, V. P., Hendershott, M. C., & Hoteit, I.: Processes governing the seasonal evolution of mixed layers in the Red Sea. Journal of Geophysical Research: Oceans, 127, e2021JC017369. https://doi.org/10.1029/2021JC017369, 2022.

Lea, D. J., Mirouze, I., Martin, M. J., King, R. R., Hines, A., Walters, D. and Thurlow, M.: Assessing a new data assimilation system based on the Met Office coupled atmosphere-land-ocean-sea ice model. Monthly Weather Review, 143, 4678-4694,.

580 doi 10.1175/MWR-D-15-0174.1, 2015

Lozier, M. S.: Evidence for large-scale eddy-driven gyres in the North Atlantic, Science, 277(5324), 361– 364, doi: 10.1126/science.277.5324.361, 1997.

Manasrah, Mohammad Badran, Hans Ulrich Lass, and Wolfgang Fennel: Circulation and winter deep-water formation in the northern Red Sea, Oceanoglica, 46(1), 5-23, 2004.

585 Morcos: Physical and Chemical Oceanography of the Red Sea, Annual Review, 8, 73-202. doi: 10.12691/ajwr-3-3-2

Morcos, and Soliman (1972), Circulation and deep water formation in the northern Red Sea in winter, *L'Océanographie Physique de la Mer Rouge, UNESCO*, 91–103, 1970

Adele K. Morrison, Darryn W. Waugh, Andrew McC. Hogg, Daniel C. Jones, Ryan P. Abernathey: Ventilation of the Southern Ocean Pycnocline, Annual Review of Marine Science 14:1, 405-430, 2022.

590 Murray, S. P., and W. Johns: Direct observations of Bab el Mandab Strait, Geophysical Research Letters 24(21), 2557-2560. doi: 10.1029/97GL02741, 1997.

OBPG, MODIS Aqua Level 3 SST Thermal IR Daily 4km Daytime v2014.0. Ver. 2014.0. PO.DAAC, CA, USA. Dataset accessed at doi: 10.5067/MODSA-1D4D4, 2015.

Papadopoulos, V. P., Y. Abualnaja, S. A. Josey, A. Bower, D. E. Raitsos, H. Kontoyiannis, and I. Hoteit : Atmospheric forcing
595 of the winter air-sea heat fluxes over the northern Red Sea, Journal of Climate, 26, 1685–1701. doi: 10.1175/JCLI-D-12-00267.1, 2013

Papadopoulos, V. P., et al.: Factors governing the deep ventilation of the Red Sea, Journal of Geophysical Research: Oceans, 120(11), 7493-7505, doi:10.1002/2015JC010996, 2015.

Patzert, W.: Wind-induced reversal in Red Sea circulation, Deep-Sea Research, 21, 109-121.doi: 10.1016/0011-
600 7471(74)90068-0, 1974.

Price, J., R. Weller, and R. Pinkel: Diurnal Cycling' Observations and Models of the Upper Ocean Response to Diurnal Heating, Cooling, and Wind Mixing Journal of Geophysical Research, 91(C7), 8411-8427. doi: 10.1029/JC091iC07p08411, 1986

Quadfasel, D., and H. Baudner: Gyre-scale circulation cells in the Red Sea, Oceanologica Acta, 16(3), 221-229, 1993.

Raitsos, D. E., Y. Pradhan, R. J. W. Brewin, G. Stenchikov, and H. I.: Remote sensing the phytoplankton seasonal succession
605 of the Red Sea, PLoS ONE, 8(6), e64909. doi:10.1371/journal.pone.0064909, 2013.

Rienecker, M. M., et al.: MERRA: NASA's Modern-Era Retrospective Analysis for Research and Applications, journal of Climate, 24(14), 3624-3648, doi:10.1175/JCLI-D-11-00015.1, 2011.

Roesler, C., Uitz, J., Claustre, H., Boss, E., Xing, X., Organelli, E., Briggs, N., Bricaud, A., Schmechtig, C., Poteau, A., D'Ortenzio, F., Ras, J., Drapeau, S., Haëntjens, N., & Barbieux, M: Recommendations for obtaining unbiased chlorophyll
610   estimates from in situ chlorophyll fluorometers: A global analysis of WET Labs ECO sensors, Limnology and Oceanography Methods 15(6), 572-585.doi: 10.1002/lom3.10185, .2017.

Sanikommu, S., Toye, H., Zhan, P.,Langodan, S., Krokos, G., Knio, O., &Hoteit, I. Impact of atmosphericand model physics perturbations on ahigh-resolution ensemble dataassimilation system of the Red Sea.Journal of Geophysical Research:Oceans,125, e2019JC015611. https://doi.org/10.1029/2019JC015611, 2020.

615   Schott, F. A., and J. P. McCreary: The monsoon circulation of the Indian Ocean, *Progress in Oceanography*, *51*(1), 1-123, doi:10.1016/S0079-6611(01)00083-0, 2001.

Smeed, D.: Seasonal variation of the flow in the strait of Bab al Mandab, Oceanologica Acta, 20(6), 773-781, 1997.

Sofianos, S., and W. Johns: An Oceanic General Circulation Model (OGCM) investigation of the Red Sea circulation, 1. Exchange between the Red Sea and the Indian Ocean, Journal of Geophysical Research 107(C11), 3196,
620   doi:10.1029/2001JC001184, 2002.

Sofianos, S. and W. E. Johns: An Oceanic General Circulation Model (OGCM) investigation of the Red Sea circulation: 2. Three-dimensional circulation in the Red Sea, Journal of Geophysical Research, 108(C3), 1-15, doi:10.1029/2001JC001185, 2003.

Sofianos, S. and W. E. Johns: Observations of the summer Red Sea circulation, Journal of Geophysical Research,
625   112(C06025), 1-20, doi:10.1029/2006JC003886, 2007.

Sofianos, S. S., W. E. Johns, and S. P. Murray: Heat and freshwater budgets in the Red Sea from direct observations at Bab el Mandeb, Deep-Sea Research Part Ii-Topical Studies in Oceanography, 49(7-8), 1323-1340, doi:10.1016/S0967-0645(01)00164-3, 2002

TEOS, SCOR, and IAPSO: The international thermodynamic equation of seawater – 2010: Calculation and use of
630   thermodynamic properties, Intergovernmental Oceanographic Commission, UNESCO, Paris, 196 pp, 2010.

Triantafyllou, G., F. Yao, G. Petihakis, K. P. Tsiaras, D. E. Raitsos, and I. Hoteit, Exploring the Red Sea seasonal ecosystem functioning using a three-dimensional biophysical model, Journal of Geophysical Research-Oceans, 119(3), 1791-1811, doi:10.1002/2013jc009641, 2014.

Werdell, P. J., et al.: Generalized Ocean color inversion model for retrieving marine inherent optical properties, Appl Optics,
635   52(10), 2019-2037, doi:10.1364/Ao.52.002019, 2013.

Williams R.G., Meijers A.: Ocean subduction, Cochran J.K., Bokuniewicz H.J., Yager P.L. (Eds.), Encyclopedia of Ocean Sciences (3rd ed.), Academic Press, Cambridge, Massachusetts, United States, pp. 141-157, 10.1016/B978-0-12-409548-9.11297-7, 2019

Woelk, S., and D. Quadfasel: Renewal of deep water in the Red Sea during 1982-1987, Journal of Geophysical Research-
640   Oceans, 101(C8), 18155-18165, doi:10.1029/96jc01148, 1996.

Yao, F., and I. Hoteit (2018), Rapid Red Sea Deep Water renewals caused by volcanic eruptions and the North Atlantic Oscillation, *Science Advances 4*(6), doi:10.1126/sciadv.aar5637.

Yao, F., I. Hoteit, L. J. Pratt, A. S. Bower, P. Zhai, A. Köhl, G. Gopalakrishnan: Seasonal overturning circulation in the Red Sea: 1. Model validation and summer circulation, J. Geophys. Res. Oceans,119, doi:10.1002/2013JC009004, 2014a.

645 Yao, F., I. Hoteit, L. J. Pratt, A. S. Bower,A. Köhl, G. Gopalakrishnan, and D.Rivas : Seasonal overturning circulation in the Red Sea: 2. Winter circulation,J. Geophys. Res. Oceans,119, 2263–2289, doi:10.1002/2013JC009331, 2014b.

Zarokanellos, N. D., B. Kürten, J. H. Churchill, C. Roder, C. R. Voolstra, Y. Abualnaja, and B. H. Jones: Physical Mechanisms Routing Nutrients in the Central Red Sea, Journal of Geophysical Research: Oceans, 122, doi:10.1002/2017JC013017, 2017a.

Zarokanellos, N. D., V. P. Papadopoulos, S. S. Sofianos, and B. H. Jones: Physical and biological characteristics of the winter-
650 summer transition in the Central Red Sea, Journal of Geophysical Research-Oceans, 122(8), 6355-6370,doi:10.1002/2017jc012882, 2017b.

Zarokanellos, N., and B. H. Jones: Winter mixing, mesoscale eddies and eastern boundary current: Engines for biogeochemical variability of the central Red Sea during winter/early spring period., Journal of Geophysical Research-Oceans, accepted, doi:10.1029/2020JC016714, 2021.

655 Zhai, P., A. S. Bower, W. M. S. Jr., and L. J. Pratt: Formation and spreading of Red Sea Outflow Water in the Red Sea, Journal of Geophysical Research, 120(9), 6542-6563, doi:10.1002/2015JC010751, 2015.

Zhan, P., G. Gopalakrishnan, A. C. Subramanian, D. Guo, and I. Hoteit: Sensitivity Studies of the Red Sea Eddies Using Adjoint Method, Journal of Geophysical Research: Oceans, 123, doi:10.1029/2018JC014531, 2018.

Zhan, P., G. Krokos, D. Q. Guo, and B. Hoteit: Three-Dimensional Signature of the Red Sea Eddies and Eddy-Induced
660 Transport, Geophysical Research Letters, 46(4), 2167-2177, doi:10.1029/2018gl081387, 2019.

Zhan, P., A. C. Subramanian, F. Yao, and I. Hoteit: Eddies in the Red Sea: A statistical and dynamical study, Journal of Geophysical Research: Oceans, 119(6), 3909-3925, doi:10.1002/2013JC009563, 2014.

Zhan, P., A. C. Subramanian, F. Yao, A. R. Kartadikaria, D. Guo, and I. Hoteit: The eddy kinetic energy budget in the Red Sea, Journal of Geophysical Research, 121(7), 4732-4747, doi: 10.1002/2015JC011589, 2016.

665 Zhang, Z., and J. C. Moore: *Mathematical and Physical Fundamentals of Climate Change*, Elsevier, doi: 10.1016/B978-0-12-800066-3.00006-1, 2015.